Synergistic transarterial electronanotherapy combining irreversible electroporation and electroconductive nanoparticles for unresectable hepatic cancer

Ratchapol Jenjob[1†], Sung-Min Jeon[1†], Yixin Jiang[2†], Enkhzaya Davaa[1], Ngoc-Thuan Truong[1,3], Jun-Hyeon Park[1,3], Eun-Bin Ji[1,3], Arjaree Jobdeedamrong[1], Nattha Suwanprakorn[1,3], Hyeong Jun Kim[4], Chiravoot Pechyen[5,6], Sitakan Natphopsuk[6,7], Tae June Kang[4], Seok Jeong[8], Su-Geun Yang[1,3,*]

1. Department of Biomedical Science, BK21 FOUR Program in Biomedical Science and Engineering, Inha University College of Medicine, Incheon 22212, Republic of Korea

2. Department of Pharmacy, Zhangzhou Health Vocational College, 12 Xiyangping Road, Zhangzhou, Fujian, 363000, People's Republic of China

3. Inha Institute of Aerospace Medicine, Inha University College of Medicine, Incheon 22332, Republic of Korea

4. Department of Mechanical Engineering, Inha University, 100 Inha-ro, Michuhol-gu, Incheon, 22212, South Korea

5. Department of Materials and Textile Technology, Faculty of Science and Technology, Thammasat University, Pathum Thani 12120, Thailand

6. Thammasat University Center of Excellence in Modern Technology and Advanced Manufacturing for Medical Innovation, Thammasat University, Pathum Thani 12120, Thailand

7. Chulabhorn International College of Medicine, Thammasat University, Pathumthani 12120, Thailand

8. Division of Gastroenterology, Department of Internal Medicine, Inha University College of Medicine, Incheon, Korea.

[†] These authors contributed equally to this work.

* Corresponding author: Su-Geun Yang. Department of Biomedical Science and Engineering, Inha University College of Medicine, Incheon, 22332, Korea. Email address: sugeun.yang@inha.ac.kr

Keywords: Irreversible electroporation (IRE), cancer electrotherapy, electroconductive dopamine nanoparticles, transarterial chemotherapy (TACE), unresectable hepatic cancer

Abstract

Rationale: Patients with unresectable hepatic cancer often have limited treatment options because the tumor anatomy complicates surgery and conventional chemotherapy shows limited activity. IRE can destroy tumor cells without heat, but complete ablation of larger tumors remains difficult. We examined whether transarterial injection of electroconductive, platinum (II)-complexed nanoparticles could improve IRE by increasing conductivity within the tumor and adding local chemotherapy.

Methods: Pt/P-Dopa NPs were injected into the tumor region before IRE. Changes in conductivity and electric-field distribution were assessed using electrochemical impedance spectroscopy in alginate hydrogel phantoms and in vivo mouse liver model. The therapeutic effect was then tested in mice with orthotopic hepatic tumors treated with IRE and transarterial Pt/P-Dopa NPs. Tumor response was assessed by MR imaging and histology.

Results: Pt/P-Dopa NPs increased electrical conductivity of alginate hydrogel phantoms from 1.64 to 5.27 mS/cm. This change produced a larger ablation volume in vivo. In tumor-bearing mice, combined IRE and nanoparticle treatment enlarged the ablation volume by approximately 31.4% and reduced tumor growth. MR imaging and histological analysis supported these findings.

Conclusions: Selective intratumoral accumulation of Pt/P-Dopa NPs maximized platinum-based chemotherapeutic activity while concentrating electroconductive effects within the tumor microenvironment. Overall, integrating chemotherapeutic and electroconductive Pt/P-Dopa NPs with IRE establishes a promising, precise, and scalable multimodal platform for locoregional therapy of unresectable hepatic cancer that warrants further translational investigation.

Introduction

Most patients with hepatic cancer are diagnosed when curative resection or transplantation is no longer possible [1]. For these patients, locoregional treatments such as transarterial chemoembolization (TACE), radiofrequency ablation (RFA), and microwave ablation (MWA) are commonly used to control intrahepatic tumors [2]. Their effectiveness, however, decreases in large, irregular, or heterogeneous lesions. Incomplete ablation leaves viable tumor cells at the treatment margin and often leads to local recurrence. Chemotherapy has similar limitations: dose-limiting toxicity, uneven drug distribution within tumors, and chemoresistance restrict its clinical benefit in hepatocellular carcinoma [3].

For locoregional cancer therapy, irreversible electroporation (IRE) offers an alternative to thermal ablation. Short high-voltage pulses, typically 800–2500 V/cm, disrupt cell membranes and induce cell death without heating the tissue [4]. Because IRE largely spares collagenous structures, blood vessels, and bile ducts, it can be applied near major vascular or biliary structures where RFA and MWA are risky [5]. When the tumor exceeds approximately 3 cm, higher voltages or more pulses may be required, but these changes can increase the risk of electrical injury [6]. Uneven tissue conductivity and irregular tumor shapes further complicate electric-field distribution, leaving portions of the tumor insufficiently treated.

One way to address this problem is to modify the electrical environment of the tumor before IRE. Transarterial delivery is particularly suitable for this purpose because anticancer agents can be introduced directly through the tumor-feeding artery. This route increases drug accumulation in the lesion and reduces

systemic exposure. If the delivered material is electrically conductive, it may also alter current pathways within the tumor and make IRE more effective.

Based on this idea, we developed a transarterial electronanotherapy strategy that combines IRE with electroconductive, drug-loaded nanoparticles [7, 8]. Specifically, we synthesized electroconductive poly(vinyl alcohol)-coated dopamine nanoparticles complexed with a cisplatin-derived platinum(II) prodrug (Pt/P-Dopa NPs). Dopamine-based nanoparticles possess the ability to coordinate metal ions such as Na^{+} (monovalent) and Mg^{2+}, Fe^{2+} (divalent), thereby functioning as electroconductive materials in aqueous environments [9-11]. Cisplatin, a widely used chemotherapeutic agent for hepatic cancer, contains a conductive platinum (Pt) center and can be readily incorporated into dopamine nanoparticles in a prodrug form, enabling efficient loading and controlled delivery. We expected that Pt/P-Dopa NPs, when administered via transarterial injection to hepatic tumors, would enhance local tissue conductivity, thereby augmenting the ablation efficacy of IRE, while simultaneously exerting a synergistic chemotherapeutic effect (Scheme 1).

To validate this hypothesis, we performed comprehensive electrochemical characterization of Pt/P-Dopa NPs in the context of IRE, including ionic conductivity measurements, impedance spectroscopy, and nanoparticle–electric field interaction analyses. These studies demonstrated that Pt/P-Dopa NPs substantially enhanced tissue conductivity and optimized electric field distribution, thereby facilitating more effective IRE-mediated ablation. The therapeutic synergy of this combination was further evaluated across two-dimensional (2D) and three-dimensional (3D) hepatic cancer cell culture models, as well as an orthotopic hepatic tumor-bearing animal model. Collectively, these in vitro and in vivo results confirmed that Pt/P-Dopa NPs significantly amplified the cytotoxic, chemotherapeutic, and ablation effects achieved by IRE alone.

Materials and Methods

Materials

Dopamine hydrochloride, 1-ethyl-3-(3-dimethylaminopropyl)carbodiimide hydrochloride (EDC), poly(vinyl alcohol) (MW 31,000 g/mol), sodium alginate, succinic anhydride, diethyldithiocarbamates (DDTC), and 4-dimethylaminopyridine (DMAP) were obtained from Sigma-Aldrich. Cisplatin was purchased from Selleck Chemicals LLC (USA). All chemical reagents were of analytical grade, obtained from commercial suppliers, and used without further purification unless otherwise specified.

Synthesis of Pt/P-Dopa NPs

P-Dopa NPs were synthesized following a reported method with modifications [9]. Specifically, dopamine hydrochloride (120 mg) was dissolved in 48 mL of deionized water under vigorous stirring. Once dissolved, 6 mL of 10% w/v PVA and 6 mL of 10 mM $KMnO_4$ solution were added to the dopamine aqueous solution and stirred at 50 °C for 4 h (Figure S1A-B). The product was then centrifuged at 30,000 rpm for 30 min and washed several times with water. To create carboxyl (-COOH) groups on the P-Dopa NPs (Figure S1C), 300 mg of succinic anhydride was dissolved in 20 mL of distilled water and stirred at 60 °C, followed by the addition of the purified P-Dopa NPs (600 mg PVA by weight). The ratio of PVA to succinic anhydride was 2:1 wt/wt [12]. The mixture was then stirred overnight, centrifuged at 30,000 rpm for 30 min, and washed several times with water to remove free succinic anhydride. Finally, the succinate P-Dopa NPs were coordinated with aquated cisplatin (Figure S1D-E). Cisplatin (0.2 mmol) was suspended in 50 mL of distilled water and mixed with 0.4 mmol of silver nitrate ($AgNO_3$) to form a cisplatin complex ($AgNO_3$/cisplatin = 2 mol/1 mol) (Figure S1E). The mixture was then stirred overnight in the dark. The AgCl precipitates formed during the reaction were removed by centrifugation at 5000 rpm for 15 min, repeated three times, and the supernatant containing the cisplatin complex, $(NH_3)_2Pt(H_2O)_2(NO_3)_2$, was collected [13]. The succinate P-Dopa NPs (Figure S1C and D) were then added

dropwise to the cisplatin complex solution and stirred at room temperature for 48 h. Finally, the mixture was purified by centrifugation at 30,000 rpm for 30 min.

Characterization of Pt/P-Dopa NPs

The size distribution and surface charges of Pt/P-Dopa NPs were measured using a Zetasizer Nano ZS (Malvern Instruments, Southborough, MA). The morphology of the particles was examined by transmission electron microscope (TEM, JEM-2100F, JEOL) and a scanning electron microscope (SEM, SU8010, Hitachi). Elemental analysis of the nanoparticles was performed using energy-dispersive X-ray (EDX) techniques. The UV-Vis absorption spectrum of Pt/P-Dopa NPs was measured using a UV-Vis spectrophotometer. The functional groups of the samples and the PVA coating on the Dopa NPs were characterized using a Fourier-transform infrared (FTIR) spectrometer (PerkinElmer, Spectrum Two). Each spectrum was scanned in the range of 4000 to 400 cm^{-1} with a resolution of 4 cm^{-1}. The loading content of Pt(II) in Pt/P-Dopa NPs was determined using inductively coupled plasma-optical emission spectrometry (ICP-OES).

Ionic conductivity of Pt/P-Dopa NPs

Alginate hydrogel phantoms were prepared to measure the ionic conductivity of P-Dopa NPs and Pt/P-Dopa NPs. Sodium alginate was dissolved in distilled water and mixed with a calcium sulfate slurry ($CaSO_4$) to obtain a 2% (w/v) alginate mixture. The $CaSO_4$ amount corresponded to 15% of the alginate carboxylate groups (Ca^{2+} ion/Alginate-COO^- ratio = 15.3 mol%). The mixture was immediately cast between glass plates separated by 3-mm spacers to form 10 × 10 × 3 mm gels. The gels were stored at 5 °C for 1 day to allow ionic crosslinking. For the conductivity measurement, the alginate solution was mixed with P-Dopa NPs (35 μg/mL) or Pt/P-Dopa NPs (50 μg/mL, containing 15 μg/mL of cisplatin and 35 μg/mL of P-Dopa NPs) and then gelled using the same method as previously described.

Ionic conductivity was measured with an electrochemical workstation (CS-310, Corrtest). A nanoparticle-loaded alginate phantom gel was placed between two stainless steel current collector plates, with the exposed area predefined as 1 cm^2 using Kapton tape (Polyimide Film Tape 5413, 3M). After stabilization of the open-circuit potential between the two stainless steel electrodes, electrochemical impedance spectroscopy (EIS) was performed over a frequency range of 0.1 Hz to 1 MHz with an AC perturbation amplitude of 10 mV. The data were fitted to an equivalent circuit model to determine the ionic conductivity. The resistance (R) of the samples was obtained from the Nyquist plot at the intercept on the real axis (Z′) in the high-frequency region, and the conductivity (σ) was calculated as follows: [14]

$$\sigma = L/A \cdot R_s \quad \text{(Eq. 1)}$$

L: thickness (3.0 mm), A: electrode area (1 cm^2), R_s: bulk resistance (Z′ value at Z″=0 obtained from the EIS).

Cell culture

Human hepatoma Hep3B cells and Hep3B cells expressing green fluorescent protein (Hep3B-GFP) were cultured in DMEM supplemented with 10% heat-inactivated FBS, 100 U/mL penicillin, and 100 μg/mL of streptomycin (Thermo Fisher Scientific, Waltham, MA) in a humidified environment at 37 °C with 5% CO_2. When the cells reached ~ 80% confluency, they were immediately used for cytotoxicity studies.

Synergistic cytotoxic effect of combination treatment

The cytotoxic effect of single treatment was evaluated on Hep3B cells using a standard protocol. Briefly, Hep3B cells were seeded into 96-well plates at a density of 2×10^3 cells per well in 0.1 mL DMEM, and incubated at 37 °C with 5% CO_2 and 90% humidity. Cells were subsequently treated with either cisplatin or Pt/P-Dopa NPs. The concentrations of Pt/P-Dopa NPs were expressed as expressed as

156 total Pt/P-Dopa NP mass concentrations. Cell viability was quantified at 24 h and 48 h post-treatment
157 using the WST-1 cell proliferation assay kit (CELLOMAX^{TM} Viability Assay kit, Seoul, Korea).

158 The combined effect of IRE and nanoparticle treatment was then examined using the same culture
159 conditions. Hep3B cells were treated with IRE (Table S1) in the presence of P-Dopa NPs (2.5 and 5 μg/ml)
160 and Pt/P-Dopa NPs (2.5 and 5 μg/ml) using BTX electroporation cuvettes (ECM 830 square wave
161 electroporation system, BTX Genetronics, CA, USA). Following a 24 h incubation, cellular viability was
162 evaluated using the WST-1 cell proliferation assay kit. Synergistic effects of combination treatment were
163 analyzed by calculating synergy scores using Combenefit software
164 (http://sourceforge.net/projects/combenefit/).

165 A colony formation assay was performed to assess the long-term effect of IRE combined with
166 Pt/P-Dopa. Hep3B cells were seeded in 6-well plates at a density of 1,000 cells per well and cultured for
167 24 h. Cells were then treated with IRE (Table S1) using plate electrodes in the presence of either P-Dopa
168 NPs (2.5 and 5 μg/mL) or Pt/P-Dopa NPs (2.5 and 5 μg/mL). Following IRE treatment, the cells were
169 further incubated for 10 days to allow colony formation. After the incubation period, colonies were fixed
170 with 4% formalin and stained with crystal violet. Plates were gently washed and dried, and the number of
171 colonies was quantified using densitometric analysis software. All data are represented as mean ± standard
172 deviation (n = 3) and analyzed by two-way ANOVA. Significance indicated as ***$P < 0.001$ and ns for
173 no significance.

174 **Observation of electrothermal effects of IRE alone and combination treatment**

175 A block-type PVA hydrogel phantom was used to compare the electrothermal induction power of
176 NPs (Dopa, P-Dopa, and Pt/P-Dopa) under IRE stimulation. The PVA hydrogel block was prepared by
177 mixing commercially available PVA hydrogel (Amos Co., Korea) with a small amount of baking soda. A
178 pair of electrodes was inserted into the hydrogel to a depth of 5 mm, and 10 μL of nanoparticle suspension,

corresponding to 10 μg of nanoparticles, was injected between the electrodes. Monophasic square wave pulses (Table S1) were delivered to the PVA hydrogel block using a DC pulse generator (ECM 830, BTX Genetronics, USA). Thermal images and temperature variations in the phantom during IRE pulse delivery were recorded using an Optris® Xi 400 infrared camera (Optris GmbH, Berlin, Germany). Statistical analysis was performed using one-way ANOVA with Tukey's multiple comparisons test (n = 3); significance was indicated as $P < 0.05$ (*), $P < 0.01$ (**), and ns (not significant).

***In vivo* hepatic ablation by IRE with portal vein-injected Pt/P-Dopa NPs in normal mice**

Male BALB/c mice (23–25 g, n = 3 / group) were assigned to the IRE-alone and Pt/P-Dopa NP combination treatment groups to evaluate hepatic ablation. Under anesthesia, a midline incision was made along the right side of the abdomen to expose the liver. PBS (100 μL) or Pt/P-Dopa NPs suspension (100 μL, 11.5 mg/mL; 1.15 mg/mouse) was injected into the portal vein in the IRE-alone and combination treatment groups, respectively. Subsequently, IRE (1,200 V/cm, 100 μs, 90 pulses) was performed using a pair of monopolar needle electrodes (21-G) inserted into the left hepatic lobe. Liver surface temperature was monitored in real time during IRE pulse delivery using a non-contact infrared camera (Optris® Xi 400, Optris GmbH, Berlin, Germany). Twenty-four hours after treatment, the livers were harvested for histological analysis and magnetic resonance imaging (MRI).

Real-time intravital fluorescence microscopic imaging for hepatic vascular injection

All animal procedures were approved by the Inha University Animal Care and Use Committee (protocol no. INHA 200820-713) and performed according to the National Institutes of Health Guide for the Care and Use of Laboratory Animals. Real-time intravital microscopy (IVM) utilizing an all-in-one system combining dual-mode confocal and two-photon microscopy (IVM-CM, IVIM Technology, Korea) was employed for in vivo visualization of hepatic tissue for injection of Pt/P-Dopa NPs [15, 16]. Orthotopic hepatic tumors were established by implanting Hep3B-GFP cells into the liver. Mice were

anesthetized and given a transvascular injection of Azure A-labeled Pt/P-Dopa NPs at a dose of 50 μg per gram of liver tissue. After 30 min, the abdomen was opened, and three-color fluorescent imaging was performed. Blood vessels, Hep3B-GFP tumor cells, and Pt/P-Dopa NPs were visualized using excitation at 405, 488, and 640 nm, respectively.

Combination treatment of IRE and Pt/P-Dopa NPs on orthotopic hepatic cancer mouse model

An orthotopic hepatic cancer mouse model was established by hemi-splenic injection of 6-week-old male BALB/c nude mice with 2×10^6 Hep3B-GFP cells per mouse (Supporting Information) [17]. Mice were randomly assigned to three groups (n = 5 per group): untreated control, IRE alone, and IRE combined with Pt/P-Dopa NPs. For the combination group, Pt/P-Dopa NPs (135 μg/mouse; 100 μL of 1.35 mg/mL) were injected into the portal vein before IRE treatment. The experimental setup was shown in Figure S2. For IRE treatment (alone or combined with NPs), a midline abdominal incision was made to expose the left liver lobe. IRE was performed using a monopolar needle electrode under the conditions listed in Table S1. Tumor response was assessed 8 days post-treatment by quantifying green fluorescent protein (GFP) expression in the treated liver lobe using an in vivo imaging system (FOBI®, NeoScience Co., Korea). Statistical significance between the untreated and IRE-alone groups was determined by Student's t-test (n = 3); ***$P < 0.001$.

Anatomical magnetic resonance imaging (MRI) of hepatic region and analysis

Approximately 24 h after IRE treatment, the livers were harvested. Six hours following harvest, anatomical MRI of the excised livers was performed using a 4.7 T system (Agilent Technologies, Santa Clara, CA, USA). Excised mouse livers were positioned in a 50-mm four-channel phased array animal coil. T2-weighted imaging sequences were acquired under conventional parameters: repetition time (TR) = 4000 ms, echo time (TE) = 37.63 ms, number of excitations (Nex) = 8, field of view (FOV) = 60 × 60 mm^2, matrix size = 256 × 256, 15 slices of 1.0 mm thickness with no gap between slices [18]. The IRE-

induced ablation zones were delineated as regions of interest (ROIs), and image analysis was performed using ImageJ (version 1.52a; National Institutes of Health, Bethesda, MD, USA).

Histological observation

Excised liver lobes were stained with 2,3,5-triphenyltetrazolium chloride (TTC) to identify the ablation lesions. Viable tissue stained red, whereas non-viable tissue within the ablated regions remained unstained. Liver sections (4 μm thick) were subjected to hematoxylin and eosin (H&E) staining for histological examination. Apoptosis was evaluated using a terminal deoxynucleotidyl transferase-mediated dUTP nick-end labeling (TUNEL) assay (G7130; Promega, USA).

Quantification of live and dead cell percentages by image analysis

Image analysis of TUNEL-stained tissue sections was performed using ImageJ 1.53c software (Wayne Rasband, National Institutes of Health, USA). Trainable Weka Segmentation was employed to create binary images that differentiated the brown-stained area (representing dead cells) from the violet-stained areas (representing live cells). The total surface area (pixel area) covered by brown signal (A_{brown}) and violet signal (A_{violet}) was calculated for each field. The relative percentages were calculated using the following equations:

$$\%\ \text{Live cells} = \left(\frac{A_{\text{violet}}}{A_{\text{violet}} + A_{\text{brown}}}\right) \times 100$$

$$\%\ \text{Dead cells} = \left(\frac{A_{\text{brown}}}{A_{\text{violet}} + A_{\text{brown}}}\right) \times 100$$

Statistical analysis

Data are presented as means ± standard deviation (SD) from at least three independent experiments. Statistical significance between groups was evaluated using Student's t-test, with p-values < 0.05 considered significant.

Results and Discussion

Characteristics of electroconductive nanoparticles: Pt/P-Dopa NPs

In this study, conductive nanoparticles (Pt/P-Dopa NPs) were developed to locally enhance electrical conductivity and improve the ablation effect of IRE. Dopa NPs were synthesized via $KMnO_4$-mediated oxidative polymerization of dopamine hydrochloride [19] and modified with PVA to obtain P-Dopa NPs. PVA is a hydrophilic and biocompatible polymer that contains numerous hydroxyl groups, which help stabilize Dopa NPs. Succinic anhydride was subsequently conjugated to P-Dopa NPs to introduce additional carboxyl groups on the nanoparticle surface. Finally, aquated cisplatin (Pt) was chemically bonded to the carboxylated P-Dopa NPs by direct mixing, forming Pt/P-Dopa NPs (Figure 1A and Figure S1).

First, P-Dopa NPs exhibited significantly enhanced colloidal stability and a narrower size distribution compared to unmodified Dopa NPs (Figure S3 and S4). The hydrodynamic diameters of Dopa NPs were approximately 485 nm (DLS) and 433 nm (SEM), while Pt/P-Dopa NPs showed a uniform diameter of ~63-69 nm by DLS, SEM, and TEM analysis (Figure 1 B-D and Figure S5). After 7 days of storage, the particle size of Dopa NPs increased from approximately 485 nm to 1500 nm, due to the aggregation of particles (Figure S6). In contrast, P-Dopa NPs and Pt/P-Dopa NPs maintained consistent sizes around 60 nm and 74 nm, respectively, over the same period (Figure 1D and Figure S7). The remarkable decrease in particle size observed after PVA surface modification can be attributed to the hydrophilic and steric stabilization provided by PVA. PVA chains, rich in hydroxyl groups, adhere onto the nanoparticle surface, preventing aggregation during the formation of Dopa NPs via both steric hindrance and hydrogen bonding with the aqueous medium, thus favoring the formation of smaller, more stable nanoparticles during the process [20, 21].

The surface charge also changed following nanoparticle modification. The zeta potential of Dopa NPs was −20 mV, compared with −9.5 mV for P-Dopa NPs and −0.5 mV for Pt/P-Dopa NPs (Figure 1E). The shift toward a near-neutral potential after cisplatin incorporation is consistent with changes in the surface chemical composition. Despite the reduced magnitude of the zeta potential, Pt/P-Dopa NPs maintained their colloidal stability during the 7-day observation period, suggesting that electrostatic repulsion was not the sole factor governing dispersion stability. Fourier transform infrared (FTIR) spectroscopy, UV-visible (UV-Vis) spectroscopy, and elemental analysis were used to characterize the nanoparticle surface and assess cisplatin incorporation. The FTIR spectrum of P-Dopa NPs showed characteristic alkyl -CH_2 stretching vibrations at 2847 cm^{-1} and 2923 cm^{-1}, supporting successful PVA coating on Dopa NPs (Figure 1F). Conjugation of cisplatin to P-Dopa NPs was further confirmed by both elemental analysis and UV-Vis absorption spectroscopy. The presence of a distinct UV-Vis absorption band for cisplatin at 280-290 nm in Pt/P-Dopa NPs was observed (Figure 1G), comparable to the absorption wavelength of free cisplatin (Figure S8) [22]. EDX mapping and elemental analysis validated the presence of platinum exclusively in Pt/P-Dopa NPs, confirming successful cisplatin incorporation; platinum was undetectable in unmodified Dopa or P-Dopa NPs (Figure 1H). ICP-OES was performed to quantify the elemental Pt content of purified Pt/P-Dopa NPs, which was determined to be 20.2 ± 0.6 wt%. This value was further converted to confirm the actual cisplatin loading content (LC) of ~31 wt% based on the molecular weight ratio of platinum in cisplatin.

Enhanced ionic conductivity of hepatic phantom after injection of Pt/P-Dopa NPs

As illustrated in Figure 2A, Pt/P-Dopa NPs were designed to improve the electrical properties of the tissue environment and thereby enhance IRE-mediated ablation. Ionic conductivity was calculated from the measured bulk resistance (R_s), sample thickness, and electrode area according to Equation 1. The ionic conductivity of Pt/P-Dopa NPs reached 5.27 mS/cm, substantially higher than that of P-Dopa NPs

(3.62 mS/cm) and the nanoparticle-free control (1.64 mS/cm; Figure 2B). These results demonstrate that the incorporation of Pt/P-Dopa NPs increased the measured ionic conductivity of the hepatic phantom. Higher conductivity may be associated with changes in ion transport and the electrical properties of the nanoparticle-containing formulation. Impedance measurements further supported these findings (Figure 2C). The real impedance (Z') increased as the frequency decreased across all tested formulations, consistent with frequency-dependent interfacial polarization. The Pt/P-Dopa NP-containing formulation exhibited the lowest Z' values over the measured frequency range. In the Nyquist plot (Figure 2D), this formulation also showed the smallest high-frequency intercept, corresponding to the lowest estimated series resistance (R_s) among the groups. The depressed semicircular response suggested non-ideal capacitive behavior within the system. Collectively, these data confirm a substantial reduction in solution resistance with Pt/P-Dopa NPs, translating to significantly enhanced electrical conductivity, which may underlie observed improvements in IRE-mediated ablation performance.

Enhanced thermal effect of IRE under combination treatment

IRE is primarily regarded as a non-thermal technique for tumor ablation. However, repeated application of high-voltage pulses can lead to localized temperature elevations in the target tissue. These thermal effects can further enhance the therapeutic efficacy of IRE by reducing tissue resistance and lowering the electroporation threshold required for nanopore formation [23]. To investigate whether Pt/P-Dopa NPs could enhance the thermal response to IRE, experiments were conducted using hydrogel phantom models (Figure 3A and 3E). The temperature increase (ΔT) was significantly greater in the Pt/P-Dopa NP group than in the control group at all measured time points. By contrast, the Dopa NP and P-Dopa NP groups showed ΔT values comparable to those of the control (Figure 3C and Figure S9). Furthermore, thermal ablation zones were notably larger in Pt/P-Dopa NP-mixed hydrogel phantoms subjected to IRE than in control phantoms treated with IRE alone (Figure 3B and Figure S10). The

elevated temperature was evenly distributed over the region between the two electrode insertion points (Figure 3D and 3H). These findings suggest that Pt/P-Dopa NPs enhanced the electrothermal response in the alginate phantom under IRE conditions. Comparable results were observed in tubular type alginate phantom models, reinforcing the reproducibility of the thermal enhancement (Figure 3E-H, and Figure S11). Notably, a Pt/P-Dopa NP concentration of 50 μg/mL was identified as an effective dose to induce thermal effects within these phantom systems (Figure 3G and Figure S11).

Synergistic cytotoxic effect of combination treatment

Synergistic combination effect of IRE and Pt/P-Dopa NPs was evaluated based on anticancer cytotoxicity studies. First, we estimated anticancer cytotoxicity of cisplatin and Pt/P-Dopa NPs treatment. An overall reduction in cancer cell viability was observed with increasing concentrations of cisplatin and Pt/P-Dopa NPs and prolonged treatment duration. At 24 h, cell viability was 82.3% with cisplatin treatment (20 μg/mL) and 62.3% with Pt/P-Dopa NP treatment (100 μg/mL, equivalent to 31 μg/mL cisplatin). At 48 h, cell viability further decreased to 39.3% and 23.3%, respectively. These results demonstrate that Pt/P-Dopa NP treatment resulted in lower cell viability than cisplatin alone at a comparable cisplatin-equivalent concentration. This suggests that the Pt/P-Dopa NPs may influence the cytotoxic effects of cisplatin on Hep3B cells.

Colony formation assays further evaluated the efficacy of combination treatment. Single IRE treatment at selected electric field strengths (800 and 900 V/cm; 20 pulses, 100 μs duration) significantly inhibited colony formation and resulted in less than 50% cell viability in Hep3B cells (Figure 4C-D). Notably, combined treatment with Pt/P-Dopa NPs and IRE at electric field of 600 V/cm and Pt/P-Dopa NP concentration of 5 μg/mL produced significantly greater suppression of colony formation than either treatment alone (Figure 4E-F). This synergistic inhibition of colony formation seems to be partly due to the release of Pt(II) from the nanoparticles and the disruption of cell membrane integrity by IRE (Figure

4, Figure S12, and Figure S13). Collectively, these findings underscore the potential of combining IRE with Pt/P-Dopa NPs as a powerful anticancer strategy in 3D Hep3B cell culture models (Figure S14). Finally, the synergistic therapeutic interaction between IRE and NPs was quantitatively evaluated using the Combenefit software. Synergy analysis based on the Highest Single Agent (HSA) model is presented in Figure 4G-H. Consistent with the cell viability data (Figure 4F), combined treatment with IRE and Pt/P-Dopa NPs led to dose- and electric field strength-dependent reductions in Hep3B cell viability. Increasing nanoparticle concentration and IRE voltage intensity correlated with greater cytotoxicity. Moreover, the combination treatment consistently outperformed each single treatment. The synergy matrices further corroborated these results: nearly all IRE treatment combined with Pt/P-Dopa NP produced positive synergy scores, indicating strong synergistic interactions (Figure 4H). In contrast, P-Dopa NP combinations exhibited some antagonistic (negative) values (Figure 4G). Notably, the highest synergy score was observed with IRE at 800-900 V/cm combined with 5 μg/mL Pt/P-Dopa NPs, suggesting this condition optimally enhances therapeutic efficacy while potentially reducing individual treatment dosages.

Intrahepatic disposition of Pt/P-Dopa NPs

In this study, we investigated the intrahepatic distribution of Pt/P-Dopa NPs following the portal vein injection (Scheme 1, Figure 5A). Azure A-labeled Pt/P-Dopa NPs (with red fluorescence, absorption peak at 650 nm) were synthesized for direct visualization of their localization within liver tissues (Figure S15). Disposition analysis was performed in both normal and orthotopic hepatic cancer mouse models (Figure 5B and 5C). In normal mice, Pt/P-Dopa NPs were observed to be evenly distributed throughout the hepatic lobules, indicating that particles with a ~70 nm diameter can efficiently penetrate hepatic parenchyma and potentially exert anticancer effects of Pt(II). In contrast, in orthotopic hepatic cancer models, Pt/P-Dopa NPs showed marked perivascular and intratumoral localization, demonstrating selective accumulation in cancerous regions. These findings underscore the dual potential of Pt/P-Dopa

NPs as both a platform for selective hepatic cancer drug delivery and as electroconductive agents for applications such as IRE-based electronanotherapy.

Enhanced ablation power of IRE under combination treatment

The enhanced ablation effect of combination treatment was evaluated by estimating ablation zone area in a normal mouse model. Analysis of TTC-stained hepatic lobes revealed that a single IRE treatment produced discrete ablation zones around each electrode, with no continuity between the anode and cathode (Figure 6A). In contrast, combination treatment with Pt/P-Dopa NPs and IRE generated the substantially largest ablation zone spanning both electrodes, with the area nearly twofold greater than that seen with IRE alone (Figure 6D). However, a moderate ablation zone was observed when P-Dopa NPs were combined with IRE, as shown in Figure S16. Notably, there was no significant difference in temperature induction (ΔT) between single IRE treatment and the combination treatment (Figure 6E) indicating that enhanced ablation was not primarily attributable to temperature elevation. The larger ablation zone following combination treatment is likely due to increased tissue conductivity conferred by Pt/P-Dopa NPs, leading to a wider spread of cell death within target regions. Histological analysis of H&E-stained tissue demonstrated more pronounced dilation of sinusoidal diameter around the central vein and greater erythrocyte congestion within dilated sinusoids with combination treatment compared to single IRE (Figure 6B). TUNEL staining revealed a higher distribution of apoptotic cells in the combination group, corroborating enhanced tumor cell death (Figure 6C). Ex vivo T2-weighted MRI was performed to assess the IRE zone size in treated liver tissue. Representative T2-weighted MR images (Figure 6F-G) show hyperintense ablation regions in both groups, with volumetric calculations based on stacked 3D images, confirming that the combination treatment led to a significantly larger ablation volume than single IRE treatment (Figure 6H). These findings collectively demonstrate that administration of Pt/P-Dopa NPs

markedly increases IRE ablation area via enhanced tissue conductivity, supporting the therapeutic potential of this combination strategy for locoregional hepatic interventions.

Therapeutic effect of combination treatment on orthotopic hepatic cancer model

Figure 7A-C demonstrates the inhibitory effect on hepatic tumor growth under each treatment, showing a reduction in the average size of tumor nodules from ~8.1 mm to ~3.4 mm in the group treated with IRE alone compared to untreated controls. In contrast, mice receiving the combination treatment of IRE with Pt/P-Dopa NPs exhibited negligible fluorescence signals, indicating a marked reduction in tumor burden. Histological analysis confirmed substantial apoptosis within tumor areas following either single IRE treatment or combination treatment, while the whole hepatic tissues remained unaffected in untreated groups (Figure 7D-G). Additionally, nuclei disruption was more pronounced in tumors treated with the combination therapy compared to IRE alone. These results demonstrate enhanced antitumor activity following the combination of IRE with Pt/P-Dopa NPs compared to IRE alone. Notably, the nanoparticle dose used in the orthotopic tumor efficacy study was lower than that used in the normal liver ablation study. Although the enhanced ablation volume was demonstrated in the normal liver model at the higher nanoparticle dose, the effect of the lower dose used in the tumor efficacy study on tissue conductivity and ablation volume remains to be determined.

To evaluate the in vivo biosafety of P-Dopa NPs, serum liver function markers (AST, ALT, ALP, and albumin) were analyzed at 2 and 4 weeks post-injection. No significant differences were observed compared with the control group, and all values remained within normal ranges (Figure S17). These results suggest no detectable hepatotoxicity within the 4-week observation period.

Conclusions

In conclusion, hepatic cancer remains a formidable therapeutic challenge with the available options often failing to achieve durable control in advanced cases. This study demonstrates an effective electro-nano-chemotherapeutic approach for overcoming treatment challenges in unresectable hepatic cancer. Integrating IRE with cisplatin-loaded electroconductive nanoparticles offers a promising advancement by significantly enhancing tumor ablation and chemotherapeutic delivery through synergistic actions in vitro and in vivo. The approach showed improved cell death and tumor inhibition by augmenting drug release and uptake during electrical stimulation. Notably, electronanotherapy provides effective, safe local tumor control, overcoming limitations of conventional thermal ablation such as the heat-sink effect and risk of damage to critical vascular structures, while minimizing systemic toxicity. Its adaptability to percutaneous and laparoscopic administration further broadens clinical utility for challenging tumor locations. Overall, these findings support the clinical potential of Pt/P-Dopa NPs-based electroporation strategies, warranting further evaluation for hepatic cancer therapy.

While the present study demonstrates that increased local conductivity significantly enhances IRE-mediated ablation, the mechanistic link between conductivity modulation and cell death signaling pathways has not been fully defined. In particular, it remains unclear how conductivity-driven changes in electric field distribution and membrane permeabilization translate into specific intracellular responses. Future studies will aim to elucidate this relationship by correlating local conductivity profiles with key molecular events, including reactive oxygen species generation, mitochondrial dysfunction, lipid peroxidation, and activation of apoptosis- and necrosis-related signaling pathways. Such investigations will provide critical insight into how bioelectrical modulation at the tissue level governs downstream biochemical and cellular responses.

Abbreviations

IRE: Irreversible electroporation; Pt/P-Dopa NPs: Platinum(IV)-complexed poly(vinyl alcohol)-coated dopamine nanoparticles; P-Dopa NPs: Poly(vinyl alcohol)-coated dopamine nanoparticles; DMEM: Dulbecco's Modified Eagle Medium; FBS: Fetal bovine serum; EDC: 1-ethyl-3-(3-dimethylaminopropyl)carbodiimide hydrochloride; DDTC: Diethyldithiocarbamates; DMAP: 4-dimethylaminopyridine; TEM: Transmission electron microscope; SEM: Scanning electron microscope; EDX: Energy-dispersive X-ray analysis; FTIR: Fourier-transform infrared spectroscopy; ICP-OES: Inductively coupled plasma–optical emission spectrometry; EIS: Electrochemical impedance spectroscopy; GFP: Green fluorescent protein.

Supplementary Material Statement

Supplementary methods, figures, and tables.

Acknowledgments

In accordance with journal and COPE guidelines, OpenAI's ChatGPT-4o was used during the preparation of this manuscript to improve English grammar, sentence structure, and overall readability. In addition, AI-assisted image generation was used to create the liver-and-tumor illustration included in the graphical abstract. No AI tools were used for study design, data collection or manipulation, **data analysis, generating experimental figures, or interpreting results.** All AI-assisted revisions were reviewed and verified by the authors, who take full responsibility for the accuracy, originality, and integrity of the published content.

Funding

This research was supported by the Basic Science Research Program, Brain Pool Program of the National Research Foundation (NRF), the Korea Medical Device Development Foundation grant funded by the Korean government (Ministry of Education and Ministry of Science and ICT, the Ministry of Trade, Industry and Resources, the Ministry of Health & Welfare, the Ministry of Food and Drug Safety), under

the following grant numbers: Grant No: RS-2024-00440714, RS-2024-00410258, RS-2026-25544148 (2410018830) and 2018R1A6A1A03025523.

Authorship contribution statement

S-GY, TJK, and SJ conceptualized the study. RJ, S-MJ, YJ, N-TT, J-HP, E-BJ, and H-JK performed the experiments. S-MJ, ED, N-TT, J-HP, and E-BJ were responsible for data acquisition, statistical analyses and conducting in vivo and in vitro experiments. RJ, S-MJ, and YJ contributed to the first draft of the manuscript. AJ, NS, CP, and SN contributed to the English editing of the manuscript. RJ, N-TT, H-JK, CP, SN, and S-GY revised the manuscript critically. All authors read and approved final version of the manuscript.

Data Availability

The data that support the findings of this study are available from the corresponding author upon reasonable request.

Competing Interests

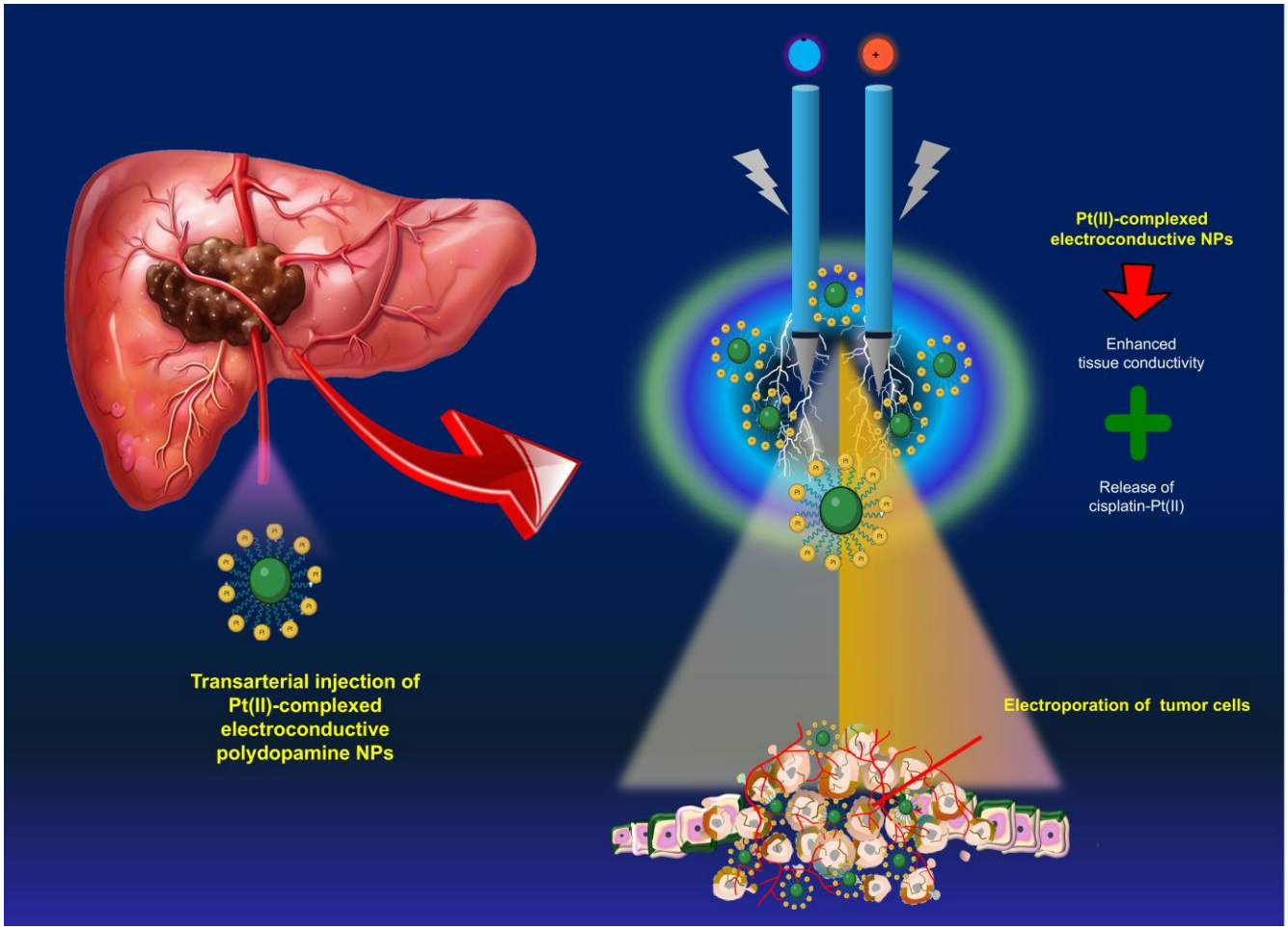
The authors declare no competing interests.

References

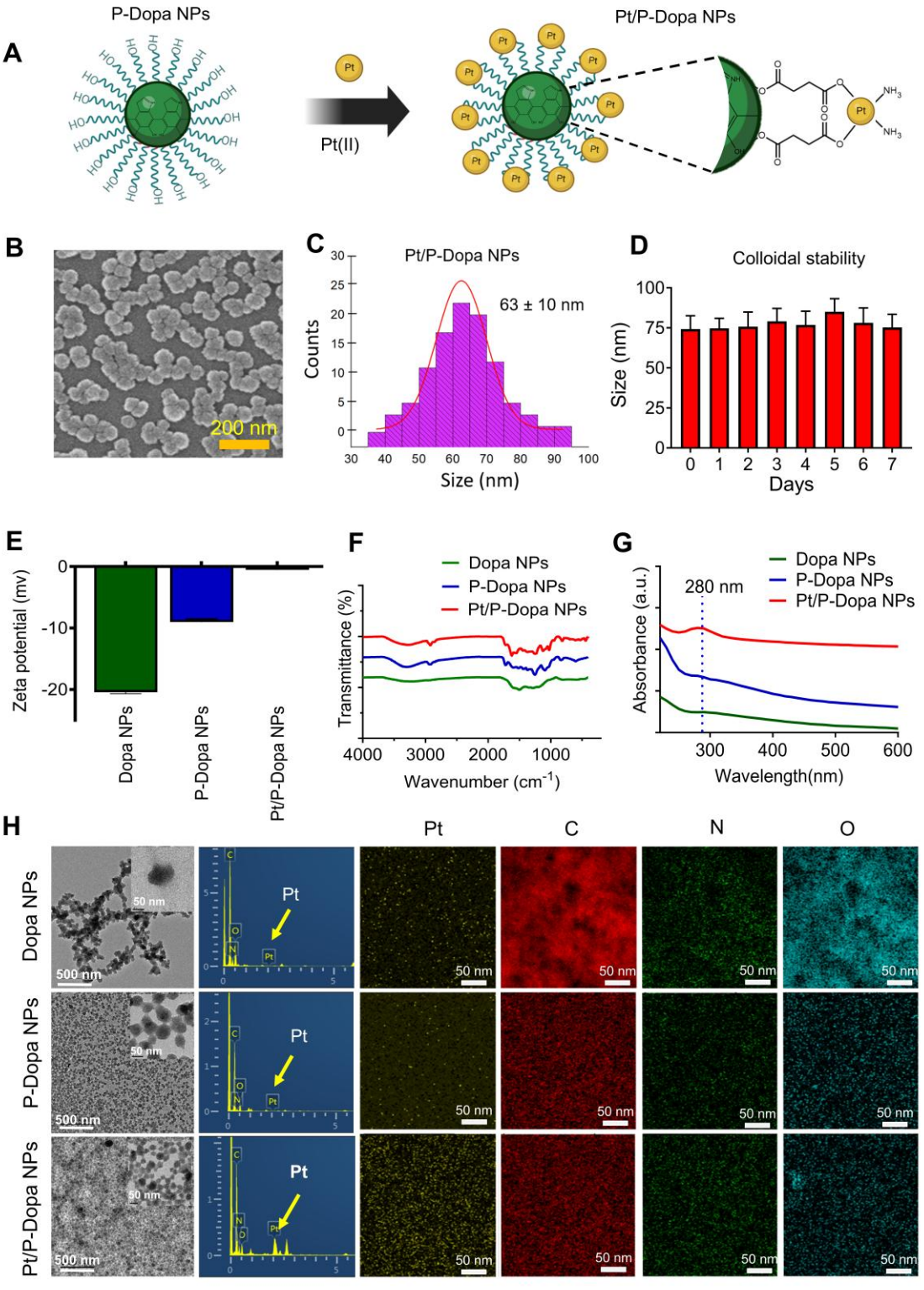
1. European Association for the Study of the L. EASL Clinical Practice Guidelines on the management of hepatocellular carcinoma. J Hepatol. 2025; 82: 315–74.
2. Ebeling Barbier C, Heindryckx F, Lennernas H. Limitations and Possibilities of Transarterial Chemotherapeutic Treatment of Hepatocellular Carcinoma. Int J Mol Sci. 2021; 22: 13051.
3. Bruix J, Chan SL, Galle PR, Rimassa L, Sangro B. Systemic treatment of hepatocellular carcinoma: An EASL position paper. J Hepatol. 2021; 75: 960–74.
4. Michel O, Kulbacka J, Saczko J, Mączyńska J, Błasiak P, Rossowska J, et al. Electroporation with cisplatin against metastatic pancreatic cancer: in vitro study on human primary cell culture. BioMed Research International. 2018; 2018: 7364539.
5. Lee EW, Chen C, Prieto VE, Dry SM, Loh CT, Kee ST. Advanced hepatic ablation technique for creating complete cell death: irreversible electroporation. Radiology. 2010; 255: 426–33.
6. Gajewska-Naryniecka A, Szwedowicz U, Łapińska Z, Rudno-Rudzińska J, Kielan W, Kulbacka J. Irreversible Electroporation in Pancreatic Cancer—An Evolving Experimental and Clinical Method. International Journal of Molecular Sciences. 2023; 24: 4381.
7. Jeon SM, Davaa E, Jenjob R, Pechyen C, Natphopsuk S, Jeong S, et al. The Induction of Combined Hyperthermal Ablation Effect of Irreversible Electroporation with Polydopamine Nanoparticle-Coated Electrodes. Int J Mol Sci. 2024; 25: 4317.

8. Jiang Y, Jenjob R, Yang SG. Enhanced Therapeutic Potential of Irreversible Electroporation under Combination with Gold-Doped Mesoporous Silica Nanoparticles against EMT-6 Breast Cancer Cells. Biosensors (Basel). 2022; 13: 41.
9. Kang S, Baskaran R, Ozlu B, Davaa E, Kim JJ, Shim BS, et al. T1-Positive Mn(2+)-Doped Multi-Stimuli Responsive poly(L-DOPA) Nanoparticles for Photothermal and Photodynamic Combination Cancer Therapy. Biomedicines. 2020; 8: 417.
10. Eom T, Lee J, Lee S, Ozlu B, Kim S, Martin DC, et al. Highly Conductive Polydopamine Coatings by Direct Electrochemical Synthesis on Au. ACS Applied Polymer Materials. 2022; 4: 5319–29.
11. Zhu M, Jia X, Li Y, Zhao C, Chao D, Wang C. A cytocompatible conductive polydopamine towards electrochromic energy storage device. Electrochimica Acta. 2021; 374: 137961.
12. Stipniece L, Salma-Ancane K, Rjabovs V, Juhnevica I, Turks M, Narkevica I, et al. Development of functionalized hydroxyapatite/poly (vinyl alcohol) composites. Journal of Crystal Growth. 2016; 444: 14–20.
13. Li J, Hu X, Liu M, Hou J, Xie Z, Huang Y, et al. Complex of cisplatin with biocompatible poly (ethylene glycol) with pendant carboxyl groups for the effective treatment of liver cancer. Journal of Applied Polymer Science. 2014; 131: 40764.
14. Eslami R, Malekkhouyan A, Santhirakumaran P, Mehrvar M, Zarrin H. Sulfonated White-Graphene for High-Performance Gel Polymer Electrolytes: The Interplay between Ion Conductivity and Rheology. Small. 2025; 21: e2410817.
15. Perrin L, Bayarmagnai B, Gligorijevic B. Frontiers in intravital multiphoton microscopy of cancer. Cancer Reports. 2020; 3: e1192.
16. Cheng SH, Li FC, Souris JS, Yang CS, Tseng FG, Lee HS, et al. Visualizing dynamics of sub-hepatic distribution of nanoparticles using intravital multiphoton fluorescence microscopy. ACS Nano. 2012; 6: 4122–31.
17. Soares KC, Foley K, Olino K, Leubner A, Mayo SC, Jain A, et al. A preclinical murine model of hepatic metastases. J Vis Exp. 2014; 51677.
18. Shangguan AJ, Zhou K, Yang J, Eresen A, Wang B, Sun C, et al. Intraprocedural transcatheter intraarterial perfusion (TRIP)-MRI for evaluation of irreversible electroporation therapy response in a rabbit liver tumor model. Clinical and experimental gastroenterology. 2020; 543–53.
19. Ryu JH, Messersmith PB, Lee H. Polydopamine Surface Chemistry: A Decade of Discovery. ACS Appl Mater Interfaces. 2018; 10: 7523–40.
20. Sahoo SK, Panyam J, Prabha S, Labhasetwar V. Residual polyvinyl alcohol associated with poly (D,L-lactide-co-glycolide) nanoparticles affects their physical properties and cellular uptake. J Control Release. 2002; 82: 105–14.
21. Kyrychenko A, Pasko DA, Kalugin ON. Poly (vinyl alcohol) as a water protecting agent for silver nanoparticles: the role of polymer size and structure. Physical Chemistry Chemical Physics. 2017; 19: 8742–56.
22. Zhang Z, Chen J, Wen T, Deng H, Zhang Y, Guo H, et al. Quantification of Cisplatin Encapsulated in Nanomedicine: An Overview. Biosensors. 2025; 15: 293.
23. Agnass P, van Veldhuisen E, van Gemert MJ, van der Geld CW, van Lienden KP, van Gulik TM, et al. Mathematical modeling of the thermal effects of irreversible electroporation for in vitro, in vivo, and clinical use: a systematic review. International journal of hyperthermia. 2020; 37: 486–505.

List of figures



Scheme 1. Schematic illustration of locoregional hepatic cancer treatment combining IRE with transarterial injection of electroconductive Pt/P-Dopa NPs. Upon the hepatic arterial injection, electroconductive Pt/P-Dopa NPs accumulate within the tumoral region, enhancing local tissue conductivity. This increased conductivity improves the electric distribution around tumor region, thereby amplifying tumor ablation power of IRE. Simultaneously, Pt(II) prodrug release provides apoptosis of hepatic cancer tissues, achieving a synergistic therapeutic effect with IRE. The liver-and-tumor illustration was generated using AI-assisted image generation, while the remaining graphical elements and overall composition were created by the authors using Microsoft PowerPoint.


A
P-Dopa NPs
Pt(II)
Pt/P-Dopa NPs
B
200 nm
C
Pt/P-Dopa NPs
63 ± 10 nm
Counts
Size (nm)
D
Colloidal stability
Size (nm)
Days
E
Zeta potential (mv)
Dopa NPs
P-Dopa NPs
Pt/P-Dopa NPs
F
Dopa NPs
P-Dopa NPs
Pt/P-Dopa NPs
Transmittance (%)
Wavenumber (cm-1)
G
Dopa NPs
P-Dopa NPs
Pt/P-Dopa NPs
280 nm
Absorbance (a.u.)
Wavelength(nm)
H
Pt
C
N
O
Dopa NPs
P-Dopa NPs
Pt/P-Dopa NPs
500 nm
50 nm

538

Figure 1. Preparation and characterizations of Pt/P-Dopa NPs. (A) Schematic illustration of Pt/P-Dopa NPs synthesis. Aquated cisplatin is coordinated with PVA shell of the P-Dopa NPs. (B) SEM image, (C) size distribution, and (D) time-dependent colloidal stability of Pt/P-Dopa NPs. (E) Zeta potential, (F) FTIR spectra, and (G) UV-Vis spectra of Dopa NPs, P-Dopa NPs, and Pt/P-Dopa NPs. (H) TEM images, EDX elemental analysis, and mapping of Dopa NPs, P-Dopa NPs, and Pt/P-Dopa NPs.

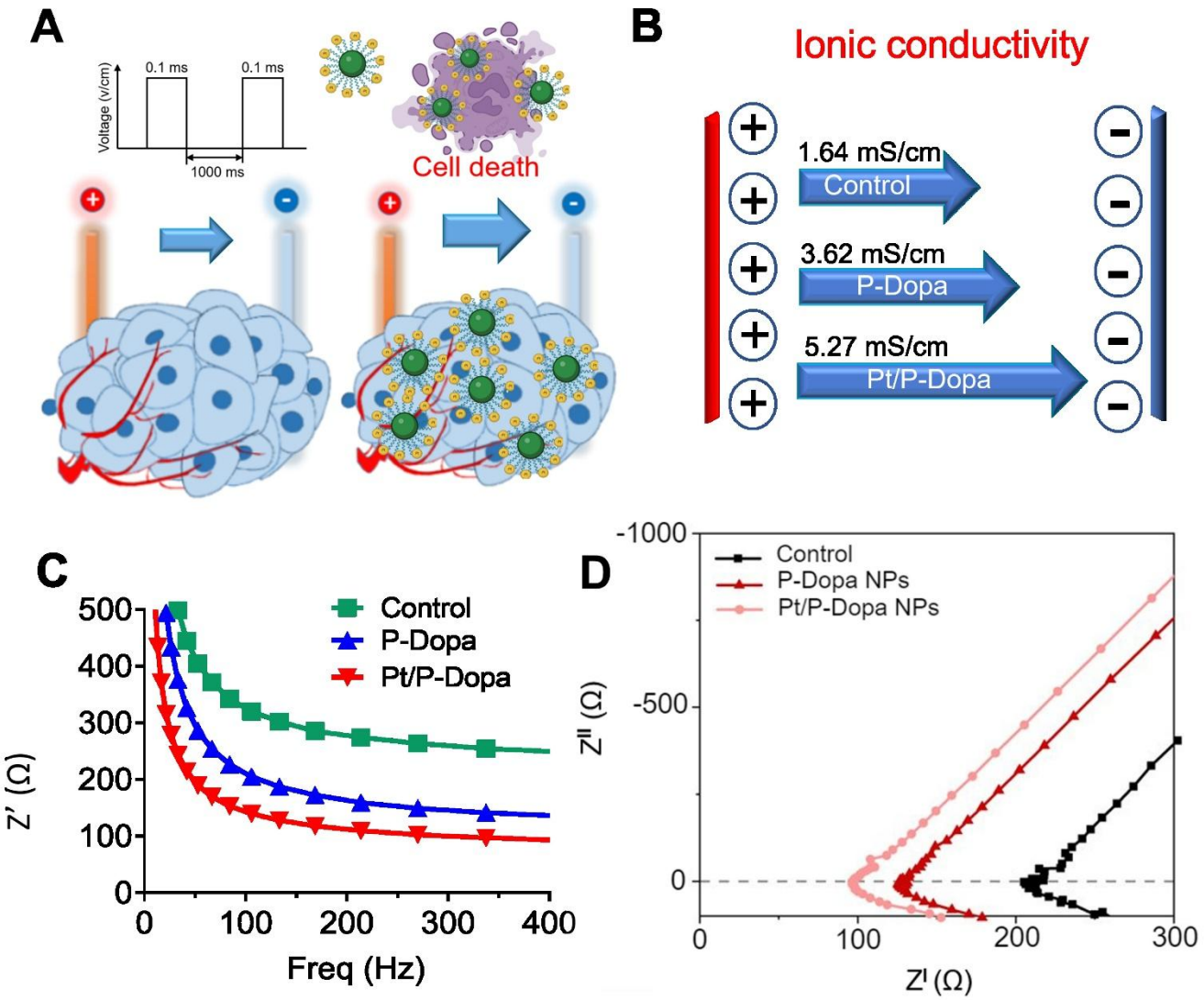


Figure 2. Enhanced ionic conductivity of Pt/P-Dopa NPs in alginate hydrogel phantom model. (A) Schematic illustration depicting the combination of IRE with electroconductive Pt/P-Dopa NPs for

locoregional hepatic cancer therapy. (B) Ionic conductivity measurements of alginate phantoms containing P-Dopa NPs and Pt/P-Dopa NPs, determined by EIS. (C) Bode plot showing the frequency dependence of the real part of impedance (Z′) for the various formulations measured from 0.1 Hz to 1 MHz. The plot specifically highlights the low-frequency region (0–400 Hz), where the most pronounced differences among groups are observed. (D) Nyquist plots comparing P-Dopa NPs and Pt/P-Dopa NPs phantoms, highlighting differences in bulk resistance.

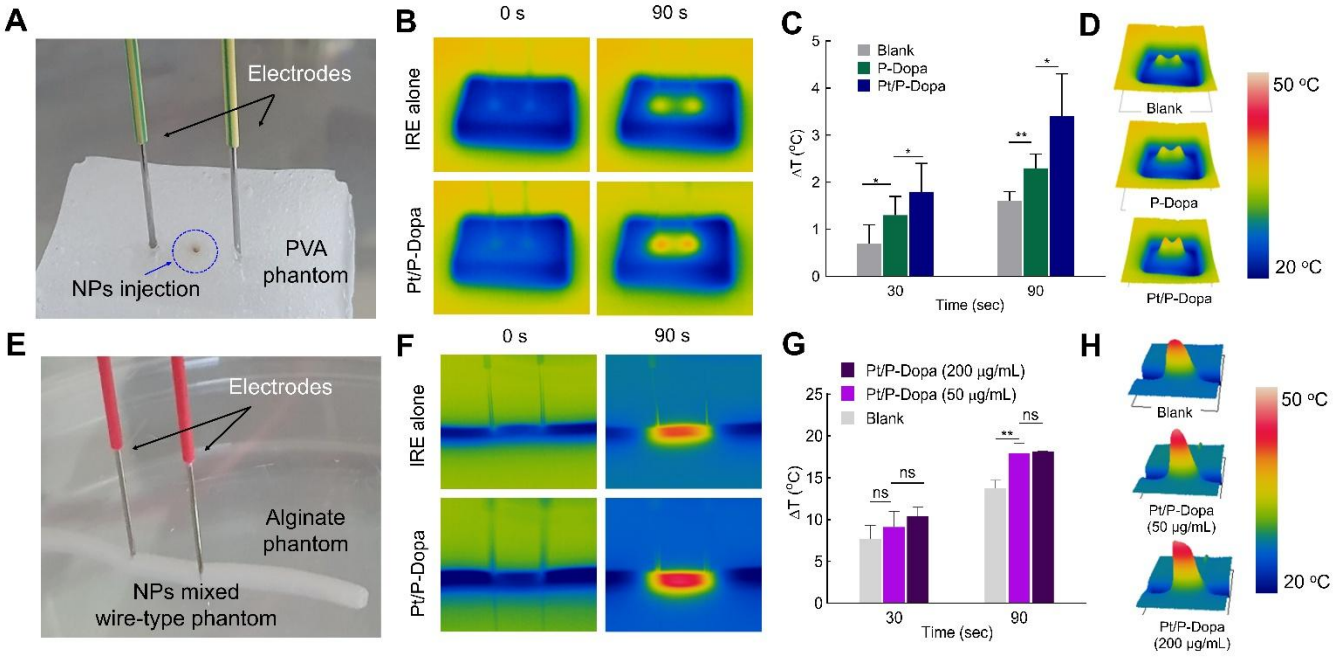


Figure 3. The enhanced thermal effect of IRE under the combination treatment with electroconductive NPs in hydrogel phantom models. (A, E) Photographs of the experimental setup for the hydrogel phantom models. Electroconductive nanoparticles were injected (or premixed) with hydrogel and introduced for IRE. (B, F) Infrared thermal images captured before and after IRE treatment. (C, G) Time-dependent temperature elevation of the phantoms during IRE treatment. (D, H) Three-dimensional infrared thermal distribution maps of phantom models. Statistical analysis was performed using one-way ANOVA (n = 3), with significance indicated as *P < 0.05, **P < 0.01, ns, not significant.

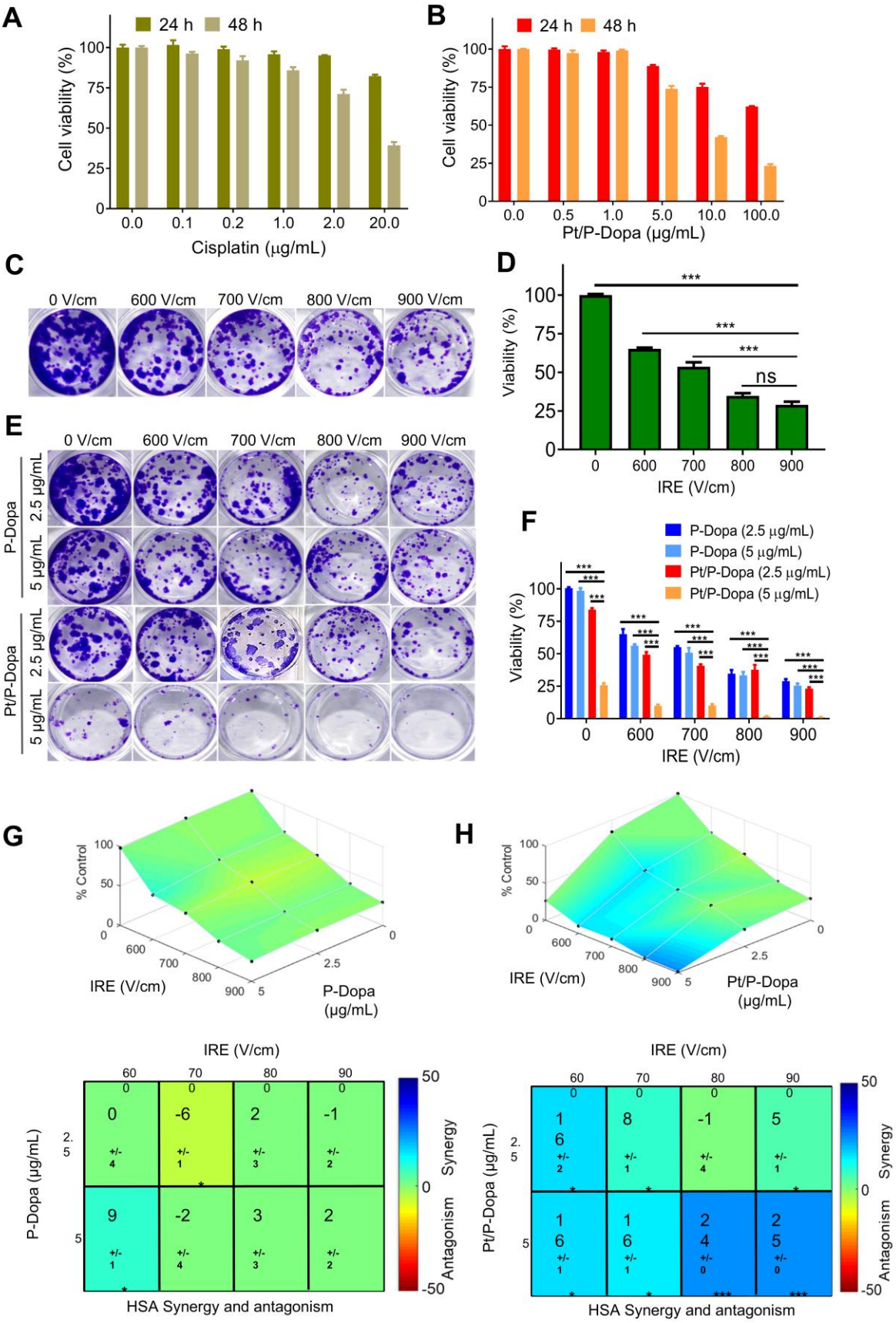
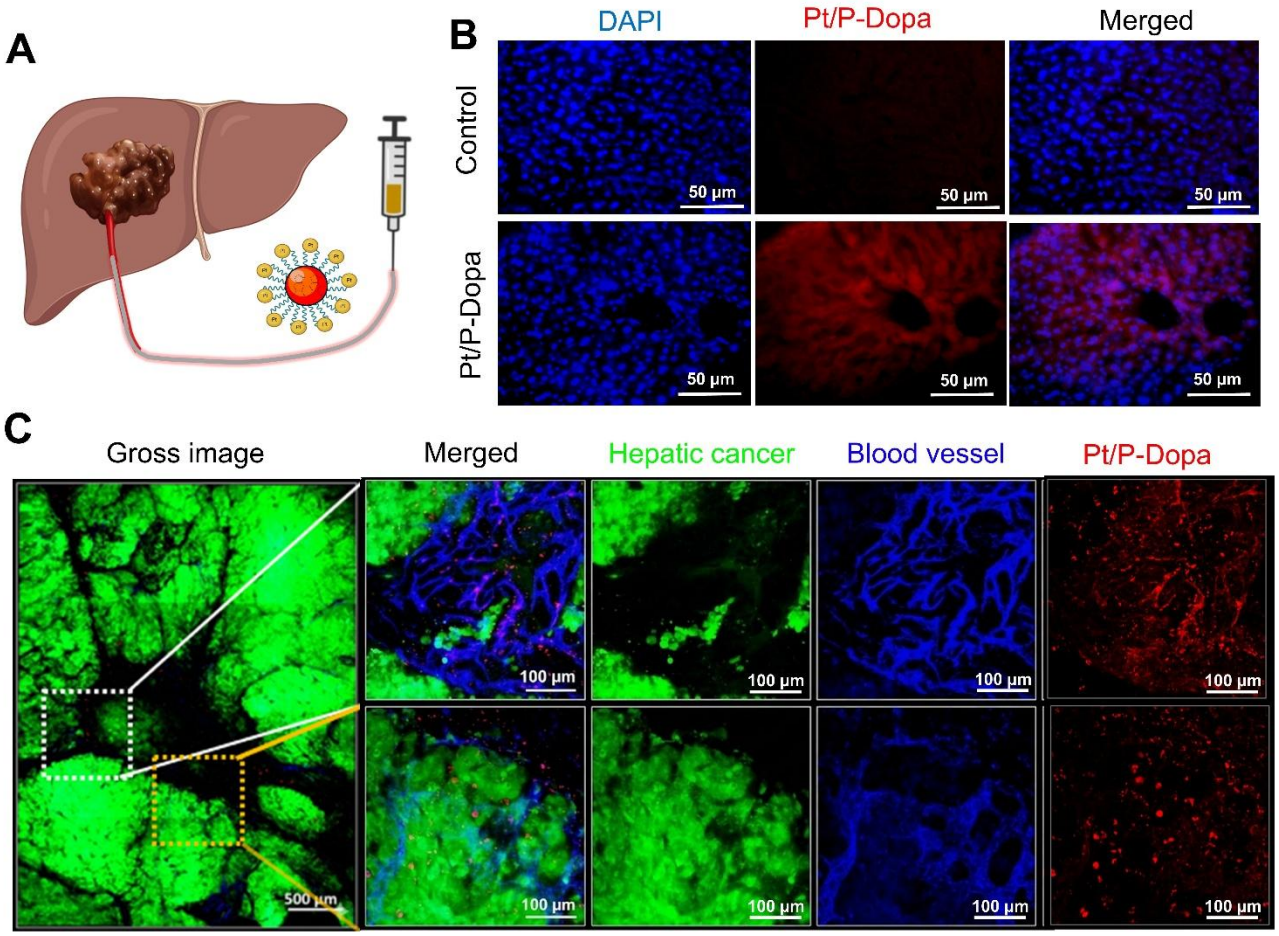

A
24 h
48 h
Cell viability (%)
Cisplatin (μg/mL)
B
Pt/P-Dopa (μg/mL)
C
0 V/cm
600 V/cm
700 V/cm
800 V/cm
900 V/cm
D
Viability (%)
IRE (V/cm)
ns
E
P-Dopa
Pt/P-Dopa
2.5 μg/mL
5 μg/mL
F
P-Dopa (2.5 μg/mL)
P-Dopa (5 μg/mL)
Pt/P-Dopa (2.5 μg/mL)
Pt/P-Dopa (5 μg/mL)
G
% Control
IRE (V/cm)
P-Dopa (μg/mL)
H
Pt/P-Dopa (μg/mL)
HSA Synergy and antagonism
Synergy
Antagonism

Figure 4. Evaluation of synergistic therapeutic effect of combination treatment. (A, B) Anticancer cytotoxicity of (A) cisplatin and (B) Pt/P-Dopa NPs in Hep3B cells at 24 and 48 h, assessed using the WST-1 assay. The concentrations of Pt/P-Dopa NPs are expressed as total Pt/P-Dopa NP mass concentrations. (C, D) Colony formation assay of Hep3B cells subjected to IRE. (E, F) Colony formation inhibition under combination treatment with IRE at the same field strengths and P-Dopa NPs or Pt/P-Dopa NPs at 2.5 μg/mL and 5 μg/mL. (G, H) Synergy analyses using Combenefit software based on HSA model, showing synergy scores for (G) P-Dopa NPs and (H) Pt/P-Dopa NPs combined with IRE at various voltages and concentrations. NPs concentrations represent total nanoparticle mass. Data represent mean ± standard deviation (n = 3). ***, $P < 0.001$, ns not significant.



573

574 **Figure 5**. **Intrahepatic disposition of Pt/P-Dopa NPs**. (A) Schematic diagram illustrating intrahepatic
575 administration of Pt/P-Dopa nanoparticles via hepatic portal vein injection. (B) Distribution of Azure A–
576 labeled Pt/P-Dopa NPs (red fluorescence) within normal hepatic tissue following portal vein infusion. (C)
577 Orthotopic hepatic cancer model established via semi-splenic injection of Hep3B-GFP cells in BALB/c
578 nude mice: hepatic cancer (green fluorescence), blood vessels (blue fluorescence), and Azure A–labeled
579 Pt/P-Dopa NPs (red fluorescence) are shown.

580

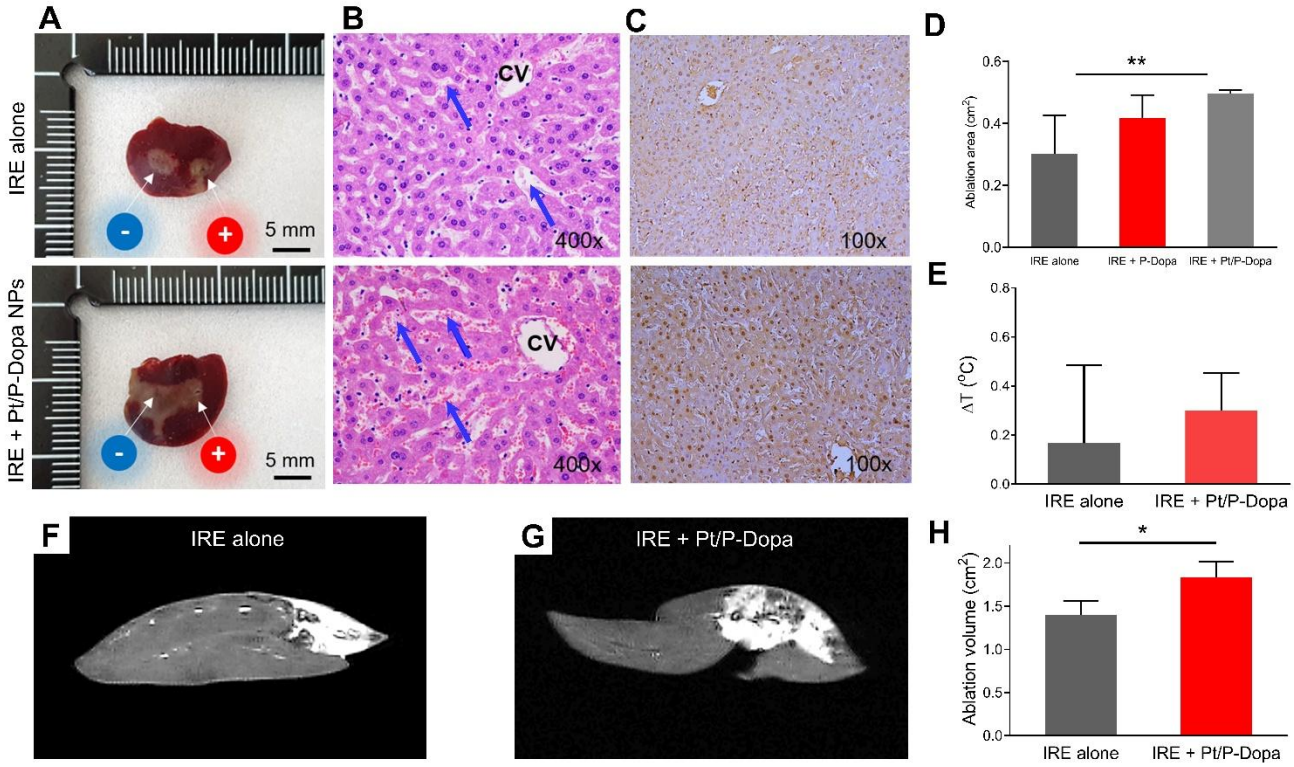


Figure 6. **Histological and MR imaging analysis of hepatic tissues following combination treatment of IRE and intrahepatic injection of Pt/P-Dopa NP**. (A) Gross and microscopic images of hepatic lobe ~~6 h~~ after single IRE treatment or combination treatment with Pt/P-Dopa NPs. (B) H&E staining illustrating differences in sinusoidal diameter (blue arrows) and blood infiltration in dilated sinusoids between groups (CV, central vein). (C) TUNEL staining showing increased apoptotic cell death (dark brown) in combination treatment compared to IRE alone. (D) Quantitative analysis of ablation area in hepatic lobes following single or combination treatment. (E) Temperature increases in the region of interest immediately after IRE treatment. Magnetic resonance imaging of hepatic lobes post-IRE: (F) single IRE treatment and (G) combination of IRE with Pt/P-Dopa NPs. (H) Quantification of ablation volume derived from three-dimensional stacked MR images. Statistical significance between groups was evaluated using an unpaired t-test (*$P < 0.05$).

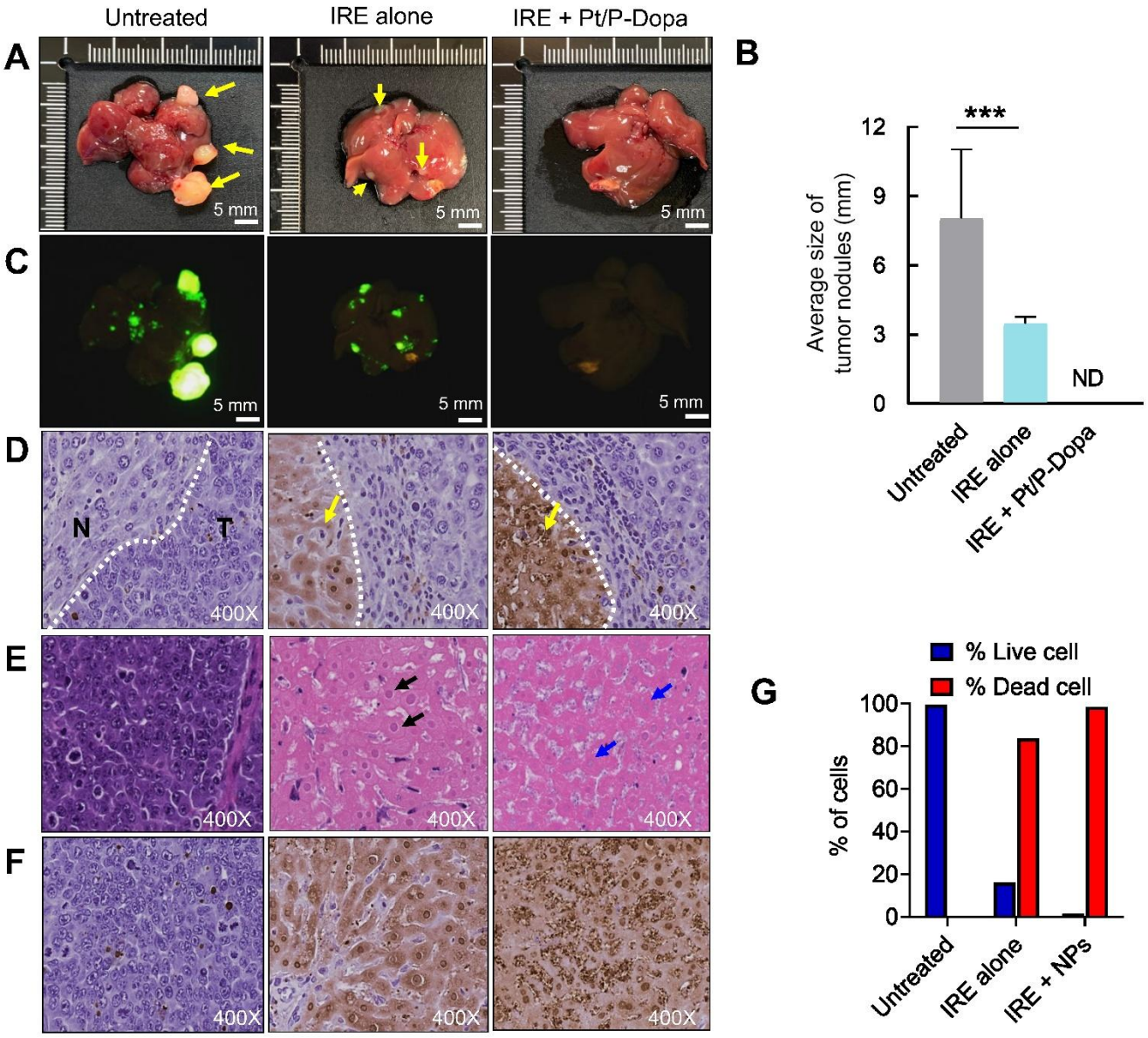


Figure 7. Combination effect of IRE and Pt/P-Dopa NPs in an orthotopic hepatic cancer mouse model after 8 days of treatment. (A) Representative gross images of whole livers showing tumor nodules (yellow arrows) in the untreated, IRE alone, and IRE + Pt/P-Dopa groups. (B) Average tumor nodule size in each treatment group. ND, not detected, indicating that no tumor nodules were detected by gross examination. (C) The representative green fluorescence images acquired from Hep3B-GFP-derived cancer nodules in the whole hepatic tissues. (D) TUNEL staining delineates the boundaries (white dotted lines) of normal hepatocyte area (N), tumor cell area (T), and the IRE ablation zone within the tumor (yellow

arrow), showing apoptosis distribution. (E) H&E staining of tumor tissue reveals aberrant nuclear morphology (blue arrows), including nuclear dissolution in the combination treatment group compared to the IRE-only group (black arrows). (F) Representative TUNEL-stained tissue sections. (G) Quantification of live and dead cell percentages based on color segmentation of TUNEL-stained images using ImageJ and Trainable Weka Segmentation. Statistical significance between the untreated and IRE-alone groups was determined by Student's t-test (n = 3); ***P < 0.001.